

# H<sub>2</sub>V<sub>3</sub>O<sub>8</sub> Nanowire/Graphene Electrodes for Aqueous Rechargeable Zinc Ion Batteries with High Rate Capability and Large Capacity

Qiang Pang, Congli Sun, Yanhao Yu, Kangning Zhao, Ziyi Zhang, Paul M. Voyles, Gang Chen, Yingjin Wei,\* and Xudong Wang\*

Aqueous rechargeable zinc ion batteries are considered a promising candidate for large-scale energy storage owing to their low cost and high safety nature. A composite material comprised of H<sub>2</sub>V<sub>3</sub>O<sub>8</sub> nanowires (NWs) wrapped by graphene sheets and used as the cathode material for aqueous rechargeable zinc ion batteries is developed. Owing to the synergistic merits of desirable structural features of H<sub>2</sub>V<sub>3</sub>O<sub>8</sub> NWs and high conductivity of the graphene network, the H<sub>2</sub>V<sub>3</sub>O<sub>8</sub> NW/graphene composite exhibits superior zinc ion storage performance including high capacity of 394 mA h g<sup>-1</sup> at 1/3 C, high rate capability of 270 mA h g<sup>-1</sup> at 20 C and excellent cycling stability of up to 2000 cycles with a capacity retention of 87%. The battery offers a high energy density of 168 W h kg<sup>-1</sup> at 1/3 C and a high power density of 2215 W kg<sup>-1</sup> at 20 C (calculated based on the total weight of H<sub>2</sub>V<sub>3</sub>O<sub>8</sub> NW/graphene composite and the theoretically required amount of Zn). Systematic structural and elemental characterization confirm the reversible Zn<sup>2+</sup> and water cointercalation electrochemical reaction mechanism. This work brings a new prospect of designing high-performance aqueous rechargeable zinc ion batteries for grid-scale energy storage.

## 1. Introduction

In the past two decades, harvesting and utilization of clean and renewable energy such as from solar and wind have experienced a very rapid evolution. Meanwhile, implementation of these intermittent energy resources imposed an immediate requirement on large-scale energy storage systems to store and regulate the power output among peak and off-peak hours. As

the most popular electrochemical energy storage device, lithium ion batteries (LIBs) are supposed to be the most promising candidate due to its high energy density. However, in such large-scale applications, cost, lifetime, and safety are particularly important factors to be considered.<sup>[1]</sup> Compared to expensive and flammable nonaqueous LIBs, aqueous batteries with water-based electrolyte possess a natural advantage in these areas. Furthermore, they do not require strict oxygen- and water-controlled manufacturing environments and thus have much lower fabrication cost. Development of aqueous battery systems progressed rapidly in recent years including monovalent Li<sup>+</sup>, Na<sup>+</sup> and K<sup>+</sup> and divalent Mg<sup>2+</sup> and Zn<sup>2+</sup> systems.<sup>[2]</sup> Among them, aqueous rechargeable zinc ion batteries (ARZIBs) attracted much attention due to the low price, rich global distribution, high stability, relatively low redox

potential and high theoretic capacity (820 mA h g<sup>-1</sup>) of zinc metal, which can be directly used as the anode material. These merits of ARZIBs substantially raised their application potential in large-scale energy storage systems and even in electric vehicles. Most recently,  $\alpha$ -MnO<sub>2</sub>,  $\beta$ -MnO<sub>2</sub>, and Zn<sub>0.25</sub>V<sub>2</sub>O<sub>5</sub>·nH<sub>2</sub>O nanofibers were successfully applied to ARZIBs with high energy density up to 250 W h kg<sup>-1</sup> and very good capacity retention over thousands of cycles.<sup>[2e–g]</sup>

In the development of high-performance ARZIBs, lack of suitable cathode materials is one of the biggest hindrances. Although the radius of Zn<sup>2+</sup> ions (0.74 Å) is almost the same as that of Li<sup>+</sup> ions (0.76 Å), the larger atomic mass and stronger positive polarity result poorer transport kinetics and lower solid-state solubility in bulk electrode. Thus, most electrode materials that can accommodate Li<sup>+</sup> ions insertion/extraction are not suitable for ARZIBs. So far, only a few cathode materials have been demonstrated in laboratory. For example, Prussian blue analogues with a cubic open-framework structure and transition metal oxides (MnO<sub>2</sub> and V<sub>2</sub>O<sub>5</sub>) with a layered structure exhibited acceptable reversible Zn<sup>2+</sup> insertion/extraction.<sup>[3]</sup> However, the former delivered limited specific capacities ( $\approx$ 60 mA h g<sup>-1</sup>) and the latter suffered from bad cycling performance. In addition to high specific capacity, other factors including morphology, structure stability, and ionic/electronic

Q. Pang, C. Sun, Dr. Y. Yu, K. Zhao, Z. Zhang, Prof. P. M. Voyles, Prof. X. Wang

Department of Materials Science and Engineering  
University of Wisconsin-Madison  
Madison, WI 53706, USA  
E-mail: xudong.wang@wisc.edu

Q. Pang, Prof. G. Chen, Prof. Y. Wei  
Key Laboratory of Physics and Technology for Advanced Batteries  
(Ministry of Education)  
College of Physics  
Jilin University  
Changchun 130012, P. R. China  
E-mail: yjwei@jlu.edu.cn

 The ORCID identification number(s) for the author(s) of this article can be found under <https://doi.org/10.1002/aenm.201800144>.

DOI: 10.1002/aenm.201800144

conductivity of the electrode materials are also critical to achieve high battery performance. For example, optimizing the crystallinity could enhance the structure reversibility. Reducing particle size and combining active materials with highly conductive additives such as carbon nanotubes or graphene could largely improve their charge–discharge rate capability. These strategies have been broadly practiced in many nonaqueous battery systems.<sup>[4,5]</sup>

Layered vanadium oxides have been considered as a promising alternative for various battery systems owing to their large interlayer distance, high theoretical specific capacity, abundant distributions, and low cost. Among them,  $\text{H}_2\text{V}_3\text{O}_8$  (or  $\text{V}_3\text{O}_7 \cdot \text{H}_2\text{O}$ ) has been reported as a promising cathode material for LIBs since 2006.<sup>[6]</sup> It is packed by  $\text{V}_3\text{O}_8$  layers (comprised of  $\text{VO}_6$  octahedrons and  $\text{VO}_5$  trigonal bipyramids) holding together by hydrogen bonds.<sup>[7]</sup> The layered structure providing a channel for easy intercalation of doubly charged  $\text{Zn}^{2+}$  ions in  $\text{H}_2\text{V}_3\text{O}_8$ . Compared to other layered vanadium oxides such as  $\text{V}_2\text{O}_5$  and  $\text{VO}_2$  which are held by weaker van der Waals interactions, the hydrogen bonds in  $\text{H}_2\text{V}_3\text{O}_8$  could offer better structural integrity and stability during charge/discharge processes. Furthermore,  $\text{H}_2\text{V}_3\text{O}_8$  has a higher electronic conductivity arising from the mixed valences of  $\text{V}^{5+}$  and  $\text{V}^{4+}$ .<sup>[8,9]</sup> Meanwhile, the high average valence (4.67) contributes more active redox sites and larger specific capacity. These unique properties suggest that  $\text{H}_2\text{V}_3\text{O}_8$  could be a promising cathode material for ARZIBs. In this study, we synthesized  $\text{H}_2\text{V}_3\text{O}_8$  nanowires (NWs) together with graphene sheets through a simple hydrothermal reaction. The as-prepared  $\text{H}_2\text{V}_3\text{O}_8$  NW/graphene composite is investigated as the cathode material for ARZIBs, which exhibited superior zinc ions storage performances including large specific capacity (up to  $394 \text{ mA h g}^{-1}$  at  $1/3 \text{ C}$ ), high rate capability ( $270 \text{ mA h g}^{-1}$  at  $20 \text{ C}$ ) and prolonged cycling stability (2000 cycles).

## 2. Characterization of $\text{H}_2\text{V}_3\text{O}_8$ NW/Graphene Composite

$\text{H}_2\text{V}_3\text{O}_8$  NW/graphene composite was synthesized via a single-step hydrothermal method (see experimental details in the Experimental Section). The crystallography of the composite was first studied by X-ray diffraction (XRD), where the characteristic peaks matched well to the orthorhombic crystalline phase of  $\text{H}_2\text{V}_3\text{O}_8$  (lattice parameters:  $a = 16.93 \text{ \AA}$ ,  $b = 9.36 \text{ \AA}$ ,  $c = 3.64 \text{ \AA}$ ,  $\alpha = \beta = \gamma = 90^\circ$ , space group:  $Pnam$ , JCPDS No. 85-2401, Figure S1, Supporting Information). A few very weak peaks between  $10^\circ$  and  $20^\circ$  were also spotted possibly due to the formation of a small amount of vanadium oxides impurities as a result of the addition of graphene oxide (GO) during the synthesis. Scanning electron microscope (SEM) images show the morphology and microstructure of the composite (Figure 1a,b).  $\text{H}_2\text{V}_3\text{O}_8$  NWs exhibited uniform sizes and a large aspect ratio with lengths of  $3\text{--}5 \mu\text{m}$  and diameters of  $50\text{--}100 \text{ nm}$ . Graphene sheets were well blended within the randomly oriented NWs forming a homogeneous mixture. The C 1s XPS spectra of  $\text{H}_2\text{V}_3\text{O}_8$  NW/graphene exhibited less oxygen-containing functional groups compared to GO (Figure S2, Supporting Information), confirming the reduction of GO to graphene.<sup>[10]</sup> This architecture ensured large contact and minimal charge traveling distance between  $\text{H}_2\text{V}_3\text{O}_8$  NWs and graphene (Figure 1c), which were favorable for optimizing the charge transport property of the composite. Transmission electron microscope (TEM) images further revealed the  $\text{H}_2\text{V}_3\text{O}_8$  NWs were anchored intimately on the graphene surface (Figure 1d). Each NW exhibited a uniform contrast showing high-quality crystallinity and negligible impurities (Figure 1e). A high-resolution TEM (HRTEM) image of the  $\text{H}_2\text{V}_3\text{O}_8$  NW displays a clear single-crystal lattice with sharp edges and no amorphous layer can be observed on the NW surface (Figure 1f). Corresponding fast

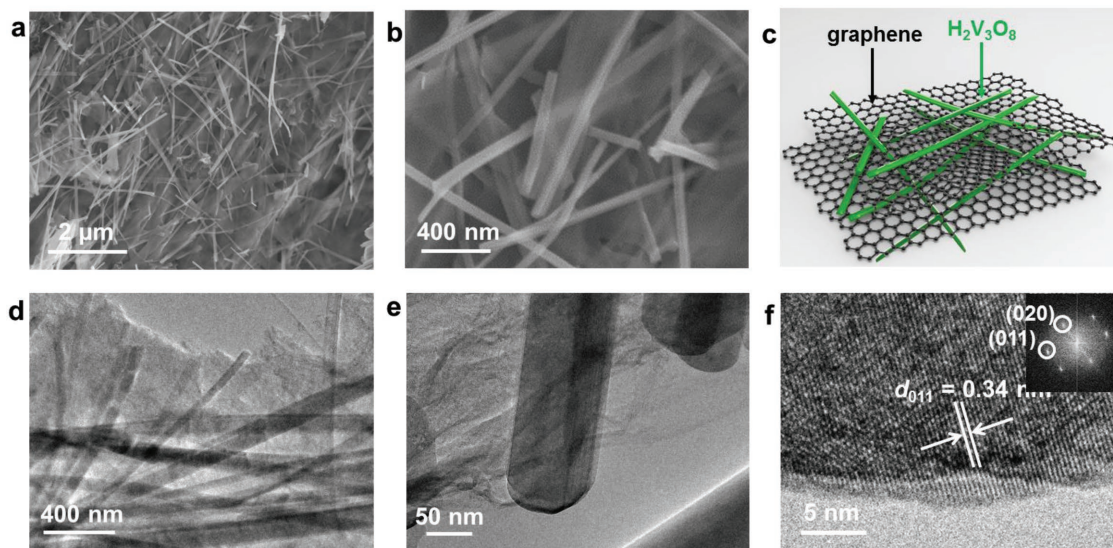


**Figure 1.** Electron microscopy characterization of the  $\text{H}_2\text{V}_3\text{O}_8$  NW/graphene composite. a) SEM image showing the morphology of the as-prepared  $\text{H}_2\text{V}_3\text{O}_8$ /graphene composite. b) SEM image depicting the intimate distribution of  $\text{H}_2\text{V}_3\text{O}_8$  NWs and graphene film. c) Schematic illustration of the structure of the composite. d) TEM image showing the uniform distribution of  $\text{H}_2\text{V}_3\text{O}_8$  NWs on graphene films. e) TEM image showing the rectangular shape of the NWs with a curve tip surface. f) HRTEM image of the NW tip showing the single-crystalline lattice of  $\text{H}_2\text{V}_3\text{O}_8$ . Inset is the corresponding FFT image.

Fourier-transform (FFT) pattern (inset of Figure 1f) revealed a *d*-spacing of 0.34 nm, which was in good agreement with the *d*<sub>011</sub> distance of H<sub>2</sub>V<sub>3</sub>O<sub>8</sub>.

H<sub>2</sub>V<sub>3</sub>O<sub>8</sub> NWs were also synthesized without adding graphene in the precursor to investigate the influence of graphene to the crystal growth. As confirmed by XRD (Figure S3a, Supporting Information), the pure H<sub>2</sub>V<sub>3</sub>O<sub>8</sub> NWs exhibited the same crystalline phase and lattice parameters with H<sub>2</sub>V<sub>3</sub>O<sub>8</sub> NW/graphene composite (Table S1, Supporting Information). SEM and TEM images revealed a small increase of NW thickness (≈50 nm in average) when no graphene was present, indicating the NW growth was slightly limited with graphene coverage (Figure S3b–d, Supporting Information). In addition, nitrogen adsorption–desorption isotherms characterization revealed that the Brunauer–Emmett–Teller (BET) surface area of the H<sub>2</sub>V<sub>3</sub>O<sub>8</sub> NW/graphene composite was 21.5 cm<sup>2</sup> g<sup>-1</sup>, which was much larger than 14 cm<sup>2</sup> g<sup>-1</sup> of the pure H<sub>2</sub>V<sub>3</sub>O<sub>8</sub> NWs (Figure S4, Supporting Information). The larger surface area can increase the contact area between the electrolyte and electrode. When dispersed in conductive additive pile for electrode preparation, the intimate contact between H<sub>2</sub>V<sub>3</sub>O<sub>8</sub> NWs and graphene was well preserved (Figure S5, Supporting Information), forming a 3D conductive graphene network with a large quantity of active materials imbedded inside. The mass fraction of graphene in H<sub>2</sub>V<sub>3</sub>O<sub>8</sub> NW/graphene composite was estimated to be ≈4.7 wt% by thermogravimetric analysis (TGA) (Figure S6, Supporting Information).

### 3. Electrochemical Performance of H<sub>2</sub>V<sub>3</sub>O<sub>8</sub> NW/Graphene in ARZIBs

The electrochemical performance of the H<sub>2</sub>V<sub>3</sub>O<sub>8</sub> NW/graphene composite electrodes was evaluated between 0.2 and 1.6 V (vs Zn/Zn<sup>2+</sup>) in coin cell-type batteries using 3 M Zn(CF<sub>3</sub>SO<sub>3</sub>)<sub>2</sub> aqueous solution as electrolyte and zinc metal foil as anode electrode. The first three charge–discharge profiles of the H<sub>2</sub>V<sub>3</sub>O<sub>8</sub>/graphene electrode at a current rate of 1/3 C (1 C = 300 mA g<sup>-1</sup>, based on the stable capacity of ≈300 mA h g<sup>-1</sup> at 300 mA g<sup>-1</sup>) are shown in Figure 2a. The first discharge capacity was 394 mA h g<sup>-1</sup>. The charge capacity was 386 mA h g<sup>-1</sup> with an initial coulombic efficiency of 98%. The high coulombic efficiency indicated good reversibility of the Zn<sup>2+</sup> ions insertion/extraction process. The discharge profiles exhibited two voltage plateaus between 0.8–0.6 V and 0.6–0.4 V, respectively. In the following charging processes, these two voltage plateaus remained in every profile. This phenomenon suggested that the electrochemical reactions might occur without irreversible crystal structure change in the subsequent cycles.

The cycling performance of the H<sub>2</sub>V<sub>3</sub>O<sub>8</sub> NW/graphene cell at current rate of 1 C after three cycles activation at 1/3 C is shown in Figure 2b. The activation process was implemented to ensure the charge/discharge reactions would occur deep (or fully) inside the electrode material lattice and thus avoid the capacity increase phenomenon during the initial cycles. The cell could deliver a specific discharge capacity of 336 mA h g<sup>-1</sup> with a 100% coulombic efficiency after 150 cycles. The rate capability of the H<sub>2</sub>V<sub>3</sub>O<sub>8</sub> NW/graphene electrode was evaluated by increasing

the current rate from 1/3 C to 10 C gradually (Figure 2c). When the current rate was increased to 5 C, the cell could still deliver a capacity as high as 240 mA h g<sup>-1</sup>. Impressively, when continue increasing the current rate from 6 to 10 C, the capacity almost remained nearly at the same value as 5 C. The specific capacities were 232, 227, 222, 218, and 215 mA h g<sup>-1</sup> from 6 to 10 C, respectively. The discharge profiles at different current rates, especially at higher current rates, showed the same shape and small polarization (Figure 2d), which evidenced the fast charge transfer kinetics of the electrode. The durability and long cycling stability at a very high current rate (20 C) of the cell was studied after the rate capability test (Figure 2e). In the first 700 cycles, the capacity gradually increased from ≈200 to 270 mA h g<sup>-1</sup> and maintained for ≈400 cycles. Then, the capacity slowly decreased to 240 mA h g<sup>-1</sup> from the 1030th to the 2000th cycle representing a high capacity retention of 87% with respect to the highest value (276 mA h g<sup>-1</sup> at 1030th cycle). Compared to other state-of-the-art ARZIB cathode materials such as β-MnO<sub>2</sub> (254 W h kg<sup>-1</sup> at 197 W kg<sup>-1</sup>),<sup>[2f]</sup> α-MnO<sub>2</sub> (≈220 W h kg<sup>-1</sup> at ≈35 W kg<sup>-1</sup>),<sup>[2e]</sup> Zn<sub>0.25</sub>V<sub>2</sub>O<sub>5</sub>·nH<sub>2</sub>O (≈170 W h kg<sup>-1</sup> at ≈30 W kg<sup>-1</sup>),<sup>[2g]</sup> ZnMn<sub>1.86</sub>O<sub>4</sub>/C (≈170 W h kg<sup>-1</sup> at ≈55 W kg<sup>-1</sup>),<sup>[11a]</sup> Na<sub>3</sub>V<sub>2</sub>(PO<sub>4</sub>)<sub>3</sub>/C (≈100 W h kg<sup>-1</sup> at ≈55 W kg<sup>-1</sup>)<sup>[11b]</sup> and Zn<sub>3</sub>[Fe(CN)<sub>6</sub>]<sub>2</sub> (≈100 W h kg<sup>-1</sup> at ≈100 W kg<sup>-1</sup>),<sup>[3b]</sup> the H<sub>2</sub>V<sub>3</sub>O<sub>8</sub> NW/graphene composite exhibited a competitive energy density and power density. Specifically, the H<sub>2</sub>V<sub>3</sub>O<sub>8</sub> NW/graphene cathode was able to deliver 168 W h kg<sup>-1</sup> at a power density of 34 W kg<sup>-1</sup> (calculated based on the total weight of H<sub>2</sub>V<sub>3</sub>O<sub>8</sub> NW/graphene composite and the theoretically required amount of Zn) and a high volumetric energy density of 325 W h L<sup>-1</sup> (calculated based on the volume of cathode electrode and theoretically required amount of Zn without considering the current collector, Figure S7, Supporting Information). The energy density still remained at a high value of 89 W h kg<sup>-1</sup> when the power density was as high as 2215 W kg<sup>-1</sup>. The weight energy density was also significantly higher than other conventional aqueous energy storage systems including supercapacitor (<10 W h kg<sup>-1</sup>),<sup>[12]</sup> aqueous lithium battery (50–80 W h kg<sup>-1</sup>)<sup>[13]</sup> and Ni-MH (20–80 W h kg<sup>-1</sup>)<sup>[14]</sup> battery. Compared to the excellent electrochemical performance of the H<sub>2</sub>V<sub>3</sub>O<sub>8</sub> NW/graphene composite, the pure H<sub>2</sub>V<sub>3</sub>O<sub>8</sub> NW electrode only showed an inferior performance including lower discharge capacity of 230 mA h g<sup>-1</sup> at 1/3 C current rate after 60 cycles and poor rate performance of only 58.4 mA h g<sup>-1</sup> at 5 C (Figure S8, Supporting Information). This comparison revealed that graphene grafting not only improved the cyclic stability and rate capability of H<sub>2</sub>V<sub>3</sub>O<sub>8</sub> NWs but also increased the discharge capacity by ≈30 mA h g<sup>-1</sup>. This enhancement can be attributed to the improved electrochemical kinetics of the electrode and the capacitive effect from the high specific area of graphene sheet.<sup>[15,16]</sup>

To reveal why the H<sub>2</sub>V<sub>3</sub>O<sub>8</sub> NW/graphene composite exhibits such a good electrochemical performance, the electrode configuration and crystal structure of the H<sub>2</sub>V<sub>3</sub>O<sub>8</sub> NW after different numbers of cycle were investigated by SEM and TEM. It was found that the composite configuration and NW morphology were preserved very well after short (Figure 3a,b) and long (Figure 3d,e) charge/discharge cycles. The graphene sheets could be clearly observed after 2000 cycles, remaining a sound distribution within the NW network (Figure 3b,e). HRTEM images further showed that the 150-cycled H<sub>2</sub>V<sub>3</sub>O<sub>8</sub>

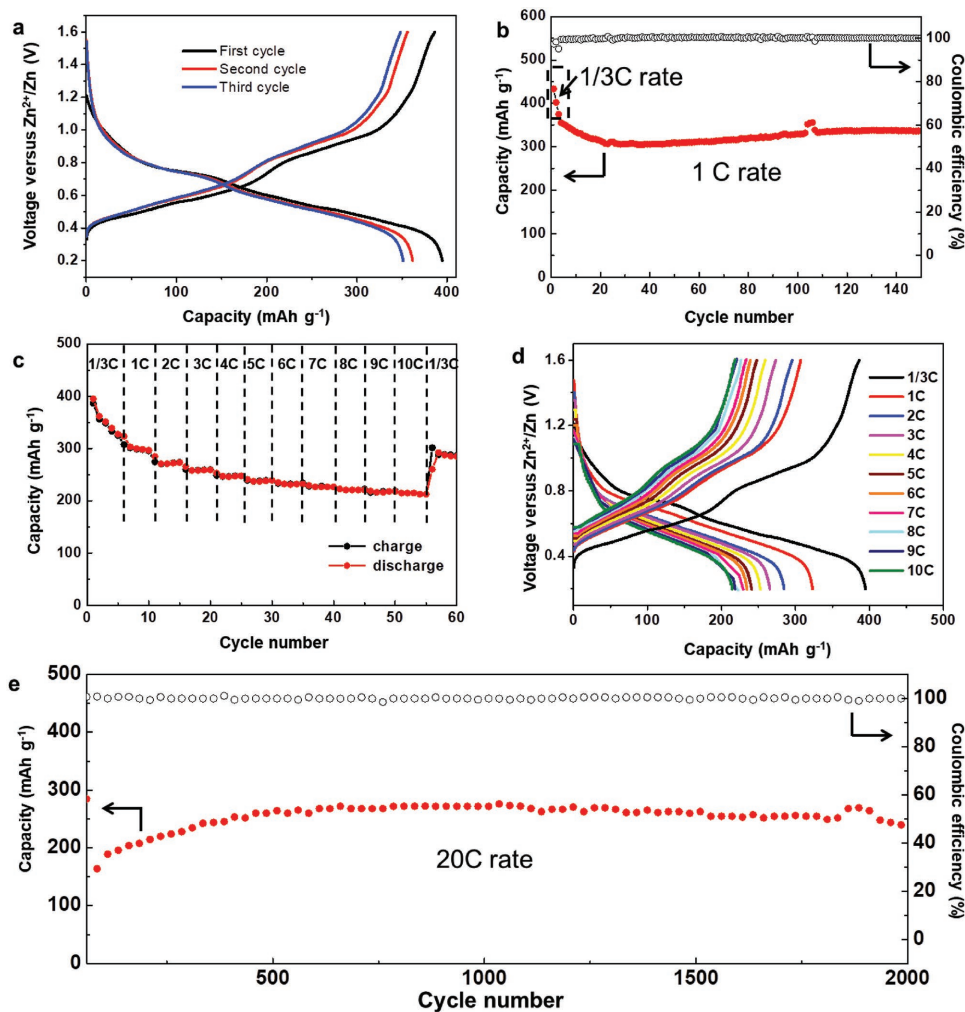


**Figure 2.** Electrochemical performance of the  $\text{H}_2\text{V}_3\text{O}_8/\text{graphene}$  electrode. a) Galvanostatic charge-discharge profiles of the the  $\text{H}_2\text{V}_3\text{O}_8/\text{graphene}$  cathode at a  $1/3$  C rate. b) Cycling performance and the corresponding coulombic efficiency at a 1 C rate after three cycles activation at  $1/3$  C rate. c) Rate capability at varying C rates. d) Galvanostatic charge-discharge profiles at different C rates. e) Long cycling stability at 20 C rate.

NWs at 1 C retained the same high quality crystal lattice as the pristine samples (Figure 3c). After 2000 cycles at 20 C, the crystalline phase of  $\text{H}_2\text{V}_3\text{O}_8$  NWs could still be clearly distinguished (Figure 3f). Accordingly, XRD spectrum of the electrode after 2000 cycles also exhibited the characteristic diffraction peaks of  $\text{H}_2\text{V}_3\text{O}_8$  (Figure S9, Supporting Information). Retaining of the  $\text{H}_2\text{V}_3\text{O}_8$  phase ensured high capacity retention during repeated charge/discharge process. However, the significantly reduced (200) peak intensity suggested that stacking of the (200) planes might become more irregularly spaced because of long-term  $\text{Zn}^{2+}$  intercalation and extraction.

Electrochemical impedance spectroscopy (EIS) was then employed to understand the electrochemical kinetics of the composite electrodes (Figure S10, Supporting Information). Nyquist plots of the  $\text{H}_2\text{V}_3\text{O}_8$  NW/graphene composite and pure  $\text{H}_2\text{V}_3\text{O}_8$  NW electrodes at the end of the first and 150th discharge all showed one semicircle, which could be assigned to the charge transfer resistance ( $R_{ct}$ ) between the electrode interface and the electrolyte. The line slope could be attributed to ion diffusion in the bulk electrode. After the first discharge,

the semicircle radius of the  $\text{H}_2\text{V}_3\text{O}_8$  NW/graphene electrode was only slightly smaller than that of the pure  $\text{H}_2\text{V}_3\text{O}_8$  NW electrode. However, after 150 cycles,  $R_{ct}$  of the  $\text{H}_2\text{V}_3\text{O}_8$  NW/graphene electrode was almost twice smaller than that of pure  $\text{H}_2\text{V}_3\text{O}_8$  NW. Such a big difference demonstrated that the graphene conductive network played a significant role in improving the charge transfer kinetics of the electrode especially after large cycling numbers.

#### 4. Mechanism of the Electrochemical Reaction

XPS was first used to investigate the electrochemical reaction of the  $\text{H}_2\text{V}_3\text{O}_8$  cathode material. As shown in Figure 4a, no Zn element signal was detected from the pristine electrode. When discharged to 0.2 V, the electrode exhibited three Zn  $2p_{3/2}$  peak components. The one located at 1023.7 eV could be attributed to the absorbed  $\text{Zn}^{2+}$  ions on the surface of graphene sheets and  $\text{H}_2\text{V}_3\text{O}_8$  NWs. Another two peaks appeared at 1026.7 and 1028.3 eV were corresponding to the intercalated  $\text{Zn}^{2+}$  with

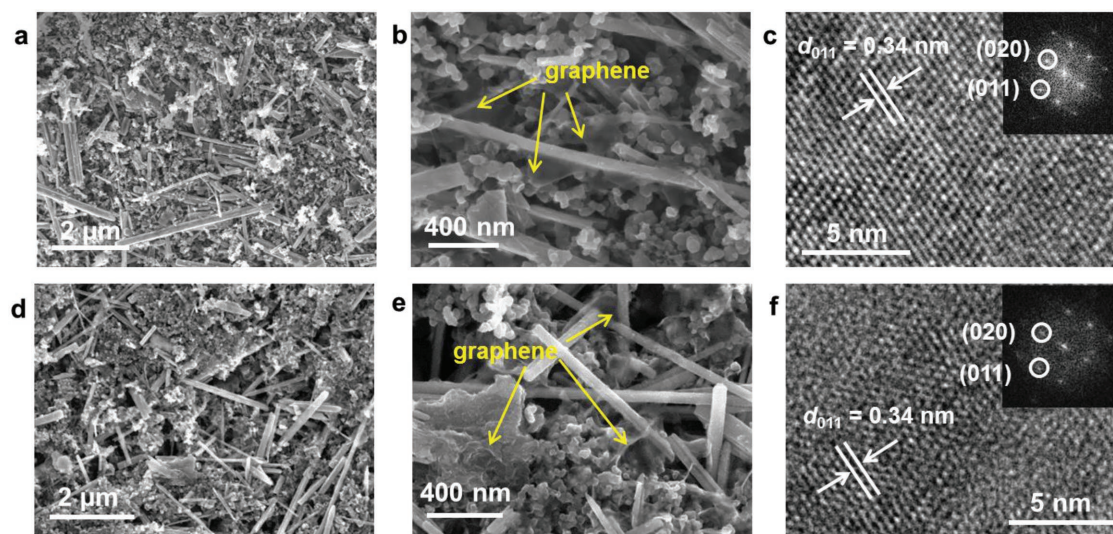


**Figure 3.** Electron microscopy investigation of the post-cycling  $\text{H}_2\text{V}_3\text{O}_8$  NW/graphene electrodes. a–c) After 150 cycles at 1/3 C rate. d–f) After 2000 cycles at 20 C rate. a,d) SEM image showing the morphology of the electrode after 150 cycles at 1/3C rate. b,e) SEM image showing the graphene conductive network in the electrode. c,f) HRTEM image of the  $\text{H}_2\text{V}_3\text{O}_8$  NW crystals.

different coordination. When the electrode was charged to 1.6 V, only a single Zn  $2p_{3/2}$  peak corresponding to surface absorption remained. This analysis suggested a reversible  $\text{Zn}^{2+}$  insertion/extraction into/from the electrode during cycling (Table S2, Supporting Information). In the pristine and fully charged electrodes, the O 1s region could be fitted into three peaks as shown in Figure 4b. The peaks located at lower energy of 529.9, 530.9, and 532.6 eV could be assigned to O 1s in  $\text{H}_2\text{V}_3\text{O}_8$ .<sup>[17]</sup> A new broad peak appeared at 533.1 eV when the electrode was discharged to 0.2 V. This peak could be assigned to O 1s from the inserted  $\text{H}_2\text{O}$  molecules.<sup>[26]</sup> Moreover, as shown in Figure 4c, the V  $2p_{3/2}$  signal in the pristine electrode could be divided into two peaks at 515.9 and 517.4 eV, corresponding to  $\text{V}^{4+}$  and  $\text{V}^{5+}$ , respectively. The peak area ratio of  $\text{V}^{4+}$  and  $\text{V}^{5+}$  was 1:2, which agreed well with the theoretical value. With the intercalation of  $\text{Zn}^{2+}$  and the reduction of  $\text{H}_2\text{V}_3\text{O}_8$ , a new peak located at 515.1 eV corresponding to  $\text{V}^{3+}$  appeared and the proportion of  $\text{V}^{4+}$  increased as the  $\text{V}^{5+}$  component decreasing.

Raman spectra in the wavelength range of 50–1200  $\text{cm}^{-1}$  recorded at different cutoff voltages were further used to analyze the electrochemical processes (Figure 4d,e). The peaks of the pristine electrode located at 141, 281.5, 410.7, 688.4, and 997  $\text{cm}^{-1}$  could be assigned to various V–O bonds in  $\text{H}_2\text{V}_3\text{O}_8$ .<sup>[18]</sup> When discharged to 0.5 and 0.2 V, a series of new peaks located at 253 and 368, 866 and 920  $\text{cm}^{-1}$  appeared. The peaks at 866 and 920  $\text{cm}^{-1}$  could be attributed to V–O vibrations in hydrated vanadium oxides.<sup>[19,20]</sup> The peaks at 253 and 368  $\text{cm}^{-1}$  were caused by the vibrations of Zn–O bonds.<sup>[21]</sup> When charged back to 1.6 V, all of the new peaks disappeared. In accordance with XPS analysis, the Raman spectra further evidence the possibility of  $\text{Zn}^{2+}$  and water coinsertion.

Ex situ XRD spectra were used to investigate the structure evolution of the  $\text{H}_2\text{V}_3\text{O}_8$  NW/graphene electrode during one charge/discharge cycle (Figure 4f). When the electrode was discharged to 0.8 V, no detectable shift of any diffraction peaks could be observed. This suggested that the structure of electrode

material during this operation period had no appreciable change when subjected to only a small amount of  $\text{Zn}^{2+}$  ions insertion. With more  $\text{Zn}^{2+}$  ions intercalated into the electrode from 0.6 to 0.2 V, a shift of peaks toward higher degree was observed. The magnified XRD curves of (200) peak were depicted in Figure S11 (Supporting Information). The corresponding reduction of the interlayer distance from 0.84 to 0.81 nm was typically believed to be a result of the enhanced electrostatic attraction between two negatively charged  $\text{V}_3\text{O}_8$  interlayers by positively charged  $\text{Zn}^{2+}$  ions intercalation.<sup>[22,23]</sup> Interestingly, when discharged to 0.5 and 0.2 V, a few new peaks appeared gradually at 6.6°, 13°, 33.6° and 38.4°. The peak located at 6.6° was corresponding to the interlayer distance of 1.34 nm. This could be attributed to the formation of a new phase with a much larger interlayer distance as reported previously.<sup>[24,25]</sup> At lower voltage, the intercalated  $\text{Zn}^{2+}$  ions triggered the insertion of water molecules, while the larger interlayer distance might further improve the ion diffusion kinetics. The charging process with extraction of  $\text{Zn}^{2+}$  ions from the electrode was the reverse of discharging. The fully charged electrode at 1.6 V showed the same pure  $\text{H}_2\text{V}_3\text{O}_8$  phase again as the pristine electrode.

Atomic-level study of the  $\text{Zn}^{2+}$  intercalation was conducted by TEM, scanning transmission electron microscopy (STEM), and electron energy loss spectroscopy (EELS) to further understand the high rate performance of the  $\text{H}_2\text{V}_3\text{O}_8$  NW/graphene electrode. In a pristine  $\text{H}_2\text{V}_3\text{O}_8$  NW shown in Figure 5a, EELS mapping showed a uniform elemental distribution of both O and V elements confirming the good stoichiometry of the NW structure. No Zn signal was detected from the pristine NW. For a  $\text{Zn}^{2+}$  ion-intercalated NW (discharged to 0.2 V, Figure 5b), while both O and V elements still remained the same intensity distribution, significant amount of Zn element signal was detected across the entire NW body with an obviously high concentration along the NW edge, indicating more  $\text{Zn}^{2+}$  ions were stored on the surface and along the edge of NW. As shown in Figure 5c, a new phase with an interlayer distance of 1.34 nm was observed

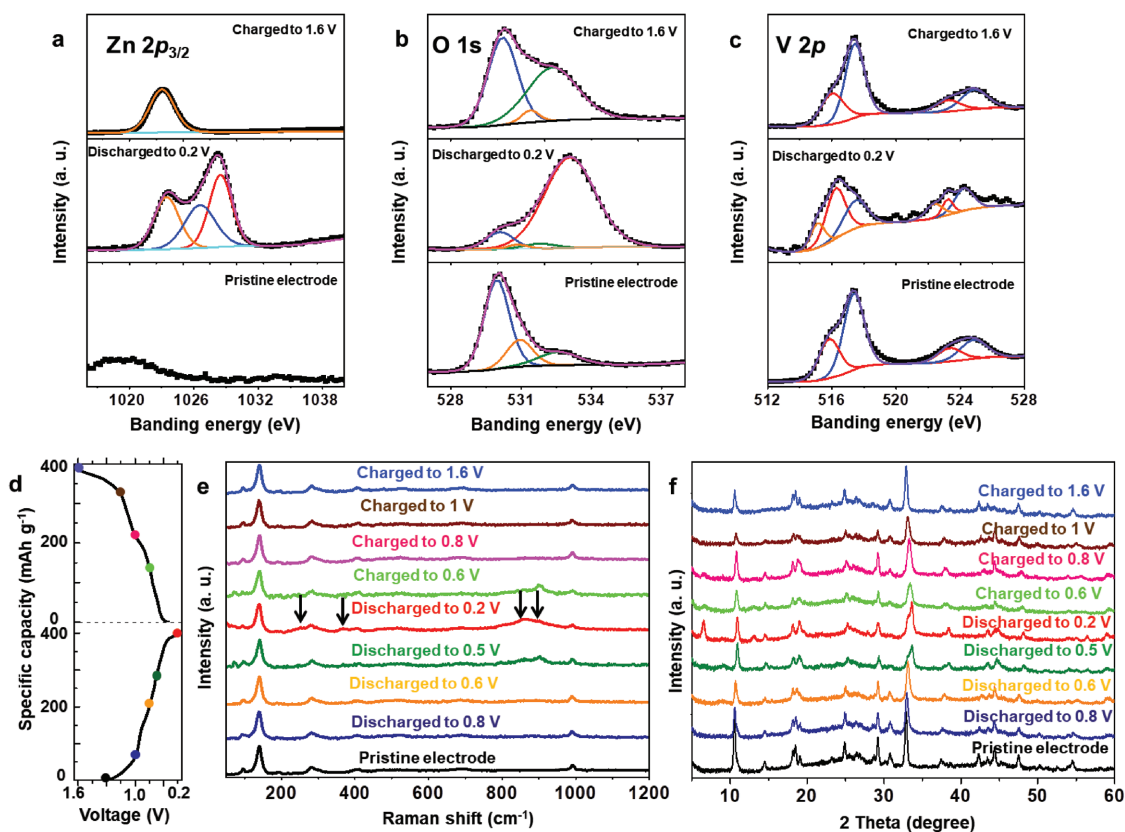


**Figure 4.** Spectroscopy investigation of the electrochemical reaction mechanism. a–c) Comparison of XPS of different elements in the composite electrode when charged to 1.6 V (top panel), discharged to 0.2 V (middle panel) and as pristine (bottom panel), for a) Zn, b) O, and c) V elements. Experimental data are shown by black lines; overall fitted data are shown by pink lines; and fitted individual peaks are shown by other colors. d) The charge/discharge curve of the first operation cycle. Sampling points for XRD and Raman characterizations were marked with corresponding colored dots. e) Raman spectrum in the wavelength range of 50–1200  $\text{cm}^{-1}$  of the electrodes. f) Ex situ XRD measurement during the first electrochemical cycle showing the reversible evolution of the  $\text{H}_2\text{V}_3\text{O}_8$  NW crystal structure.

distributing longitudinally along the NW axial direction (Figure 5d). This lattice spacing corresponds well to the new XRD peak at  $6.6^\circ$ . Other part of the NW still remained the original  $\text{H}_2\text{V}_3\text{O}_8$  phase with negligible change of the lattice spacing of the (011) plane (Figure 5e). There were also NWs remained the pure  $\text{H}_2\text{V}_3\text{O}_8$  phase (Figure 5f; Figure S12, Supporting Information). The slightly reduced (200) d spacing (0.82 nm) was in good agreement with the XRD peak shift (Figure S11, Supporting Information). The mixed final phase might be the reason of the different crystal evolution and electrochemical behaviors compared to those discovered from the pure-phased  $\text{Zn}_x\text{V}_2\text{O}_5 \cdot n\text{H}_2\text{O}$  cathode materials.<sup>[2g]</sup> High-precision high angle annular dark field (HAADF) STEM experiments were further acquired from the  $\text{H}_2\text{V}_3\text{O}_8$  phase region following approaches developed by Yankovich.<sup>[26]</sup> The STEM image series was acquired 300 frames using  $512 \times 512$  pixels and the pixel dwell time was  $\approx 2 \mu\text{s}$ . As shown in Figure 5g, additional HAADF signals could be observed inside some quasi-hexagons of V atoms (yellow arrows). Figure 5h shows the intensity line scan along the dashed line in the HAADF image. Clear shoulders could be observed adjacent to the V dumbbells, which were likely to be intercalated  $\text{Zn}^{2+}$  sites. Density functional theory (DFT) calculation showed that Zn is stable at the center of the vacant sites, with slight distortion to neighboring V atoms (Figure 5i,j). This was also observed in

the HAADF image. From a 2D Gaussian fitting with projected interatomic distances marked (Figure S14, Supporting Information), additional Zn HAADF signal could be located inside the V quasi-hexagon, together with a slight distortion of neighboring V atoms. STEM analysis and DFT calculation suggested that the rows of vacancy sites between V–O octahedrons could accommodate the intercalation of  $\text{Zn}^{2+}$  ions with very small lattice distortion, offering fast  $\text{Zn}^{2+}$  diffusion channels with minimal kinetic energy barrier, and thus the ultrahigh rate capability.

## 5. Conclusion

In this work, we developed a novel  $\text{H}_2\text{V}_3\text{O}_8$  NW/graphene composite as a promising cathode material for ARZIBs. The composite was synthesized by a one-step hydrothermal method, offering a great potential for low-cost and large-scale manufacturing. This one-step synthesis strategy enabled a uniform mixture and intimate contact between the  $\text{H}_2\text{V}_3\text{O}_8$  NWs and graphene surfaces, which significantly improved the charge transfer kinetics and stability of the composite electrode. The high quality  $\text{H}_2\text{V}_3\text{O}_8$  NW crystal structure allowed rapid and reversible  $\text{Zn}^{2+}$  intercalation/extraction. Therefore, the  $\text{H}_2\text{V}_3\text{O}_8$  NW/graphene composite exhibited a large specific capacity of

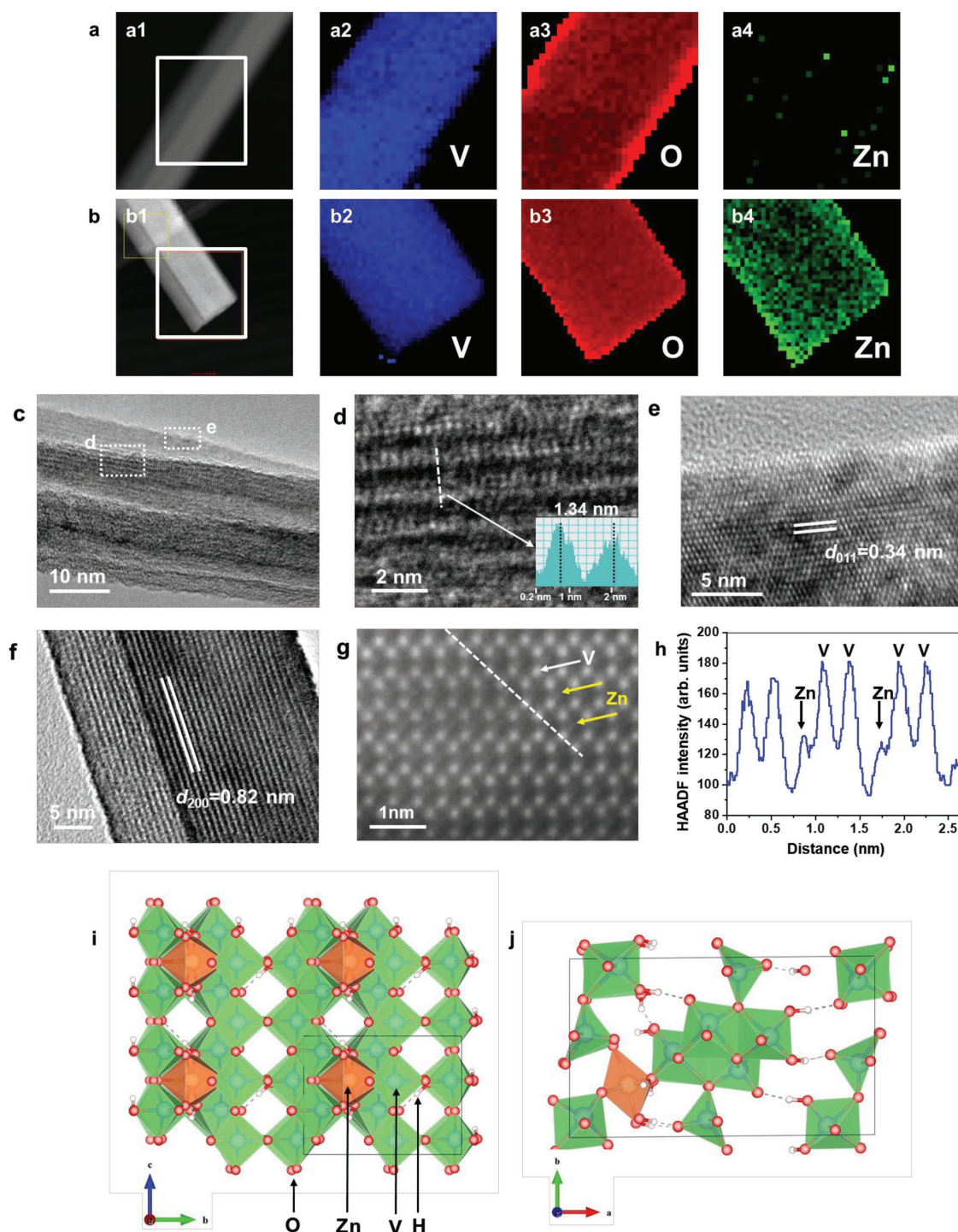


**Figure 5.** Atomic-level study of the  $\text{Zn}^{2+}$  intercalation in  $\text{H}_2\text{V}_3\text{O}_8$  NWs. a) EELS mapping of a pristine  $\text{H}_2\text{V}_3\text{O}_8$  NW. The white box shows the region used for EELS mapping (a1). The V element (a2). The O element (a3). No Zn element signal was detected in the NW (a4). b) EELS mapping of a zinc-intercalated  $\text{H}_2\text{V}_3\text{O}_8$  NW discharged to 0.2 V. The white box shows the region used for EELS mapping (b1). The V element (b2). The O element (b3). The Zn element (b4). c) TEM image of a  $\text{H}_2\text{V}_3\text{O}_8$  NW discharged to 0.2 V. d) HRTEM image of the new phase within the NW. Inset is the intensity profile along the dashed line. e) HRTEM image of the unchanged  $\text{H}_2\text{V}_3\text{O}_8$  phase region. f) HRTEM image of a discharged  $\text{H}_2\text{V}_3\text{O}_8$  NW showing the  $d_{200}$  lattice spacing. g) High-precision HAADF STEM image of a  $\text{H}_2\text{V}_3\text{O}_8$  NW discharged to 0.2 V. h) Intensity line scan along the white dashed line in the HAADF image (Figure 5c). i, j) Potential intercalated Zn sites in the  $\text{H}_2\text{V}_3\text{O}_8$  crystal viewed along the [100] direction (e) and along the [001] direction (f).

$394 \text{ mA h g}^{-1}$  at 1/3 C, a high-rate capability of  $270 \text{ mA h g}^{-1}$  at 20 C and excellent cycling stability of more than 2000 cycles. The crystal evolution and electrochemical mechanism of  $\text{Zn}^{2+}$

and water cointercalation were systematically investigated by ex situ XRD, Raman and XPS spectra. HRTEM image revealed the emergence of a new phase with a large interlayer spacing

as a result of coinsertion of  $\text{Zn}^{2+}$  ions and water molecules. STEM analysis suggested that the  $\text{Zn}^{2+}$  ions were located at the vacancy sites between V–O octahedrons, which might be responsible for the ultrahigh rate capability. Combining the advantages of zinc metal anode and mild-acidic aqueous electrolyte, this ARZIB system holds a great potential for large scale energy storage applications with low price, excellent safety, and high durability.

## 6. Experimental Section

**Material Synthesis:** Graphene oxide was produced from natural graphite (<20 mm; Sigma-Aldrich) using a modified Hummers method.<sup>[27]</sup> Graphite powder (2.0 g) was added to a mixture of  $\text{H}_2\text{SO}_4$  (98 wt%, 8 mL),  $\text{K}_2\text{S}_2\text{O}_8$  (1.67 g), and  $\text{P}_2\text{O}_5$  (1.67 g). This mixture was kept at 80 °C for 5 h. Subsequently, the mixture was cooled to room temperature and diluted with deionized (DI) water (0.5 L). After being filtered and washed several times with DI water, the suspension was dried under ambient conditions. This preoxidized graphite was treated with  $\text{H}_2\text{SO}_4$  (98 wt%) in ice water. Next,  $\text{KMnO}_4$  (15.0 g) was added to the treated graphite suspension gradually with constant stirring at 35 °C for 2 h. Shortly after dilution with water (0.7 L),  $\text{H}_2\text{O}_2$  (30%, 20 mL) was added to the mixture, which was then washed with HCl followed by DI water. The GO powder was finally obtained after centrifugation, copious washing with DI water, and freeze drying. For preparing the GO solution, 50 mg of the as-synthesized GO powder was dispersed in 21 mL DI water uniformly under ultrasonic for 2 h.

$\text{H}_2\text{V}_3\text{O}_8$  NWs and  $\text{H}_2\text{V}_3\text{O}_8$  NW/graphene composite were prepared by a hydrothermal method. In a typical synthesis,  $\text{V}_2\text{O}_5$  powder (0.364 g) was added to DI water (20 mL) and the mixture was stirred vigorously. Then,  $\text{H}_2\text{O}_2$  (4 mL) was added to the solution, which was stirred constantly for another 2 h. Subsequently, 20 mL GO solution was added to 14 mL of the mixture under vigorous stirring, followed by 6 h ultrasonication. Finally, the solutions were transferred to a 50 mL autoclave and kept in an oven at 200 °C for 5 d. The product was washed several times with ethanol and DI water, and then dried at 60 °C to obtain the  $\text{H}_2\text{V}_3\text{O}_8$  NW/graphene composite material. For comparison, pure  $\text{H}_2\text{V}_3\text{O}_8$  NWs were prepared through the same hydrothermal procedure without adding the GO solution.

**Characterizations:** XRD (Bruker D8, Bruker, MA, USA) was implemented to study the crystal structure. SEM observations were performed on a Zeiss LEO 1530 field-emission microscope and TEM and HRTEM measurements were conducted on a FEI TF30 microscope. Raman scattering data were collected on a Thermo Scientific FT-Raman spectrometer using an Nd-line laser source. Nitrogen adsorption–desorption isotherms were measured on a Micromeritics ASAP 2010 instrument. XPS scan was acquired using a Thermo Scientific K-alpha XPS instrument. STEM and EELS experiments were performed on a FEI Titan microscope with a CEOS probe aberration-corrector operated at 200 keV. The probe semiangle is 24.5 mrad and the probe current is  $\approx 25$  pA. HAADF STEM imaging was collected by a Fischione Model 3000 detector spanning 84 to 160 mrad in scattering angles. In these conditions the estimated probe size is less than 1 Å. EEL spectrum image were recorded with GIF 865 spectrometer, with energy dispersion of 1 eV per pixel, which allows for the simultaneous visualization of the V L, O K, and Zn L EELS edges. The energy resolution was 1.2 eV measured from the full width at half maximum of zero-loss peak. TGA was measured by a TA Q500 thermogravimetric analyzer. pH of the electrolyte was measured using a PHS-300 pH meter.

**Electrochemical Measurements:** Electrochemical experiments were performed using 2016 coin cells in the voltage window of 1.6–0.2 V and a metallic Zn foil used as the counter electrode. The working electrode was composed of 70 wt% active materials, 20 wt% Super P conductive additive, and 10 wt% polyvinylidene difluoride binder, and was coated on a Ti foil current collector. The electrodes for XRD and XPS measurements were prepared by using poly tetra fluoroethylene

as binder and rolling to a sheet. The electrode was cut into pieces  $5 \times 5 \text{ mm}^2$  in size and the loading density was about  $1 \text{ mg cm}^{-2}$ . The working and counter electrodes were separated by a Whatman GF/C glass fiber filter. The electrolyte was 3 M  $\text{Zn}(\text{CF}_3\text{SO}_3)_2$  aqueous solution (pH 3.55) because much better electrochemical performance has been discovered from the 3 M  $\text{Zn}(\text{CF}_3\text{SO}_3)_2$  electrolyte compared to other concentrations and other Zn salts such as  $\text{ZnSO}_4$ ,  $\text{Zn}(\text{NO}_3)_2$  and  $\text{Zn}(\text{ClO}_4)_2$ .<sup>[2f,11a]</sup> 5 vol% diethyl ether was added in the electrolyte to improve the stability of Zn metal in aqueous electrolyte.<sup>[28]</sup> Galvanostatic charge–discharge cycling was performed on a Land-2100 battery tester. The capacity of the samples was calculated based on the weight of  $\text{H}_2\text{V}_3\text{O}_8$  and graphene for the  $\text{H}_2\text{V}_3\text{O}_8$  NW/graphene composite electrode and the weight of  $\text{H}_2\text{V}_3\text{O}_8$  for the pure  $\text{H}_2\text{V}_3\text{O}_8$  NWs electrode. EIS was obtained by applying an AC voltage of 10 mV in the frequency range from 1 MHz to 1 Hz using an Autolab PGSTAT302N station. Before XRD and XPS measurements, the free standing electrodes at different charge/discharged stages was immersed and washed thoroughly in DI water and dried at 60 °C in air.

## Supporting Information

Supporting Information is available from the Wiley Online Library or from the author.

## Acknowledgements

This work was primarily supported by U.S. Department of Energy (DOE), Office of Science, Basic Energy Sciences (BES), under Award # DE-SC0008711. Q.P. thanks the financial support from the China Scholarship Council scholarship. STEM characterization (C.S. and P.M.V.) was supported by the US Department of Energy (DE-FG02-08ER46547). Facilities for microscopy and spectroscopy were supported by the University of Wisconsin-Madison Materials Research Science and Engineering Center (DMR-1720415)

## Conflict of Interest

The authors declare no conflict of interest.

## Keywords

aqueous rechargeable zinc ion batteries, cathode materials, energy storage, graphene composites,  $\text{H}_2\text{V}_3\text{O}_8$  nanowires

Received: January 13, 2018

Published online:

- [1] J. Liu, J. Zhang, Z. Yang, J. P. Lemmon, C. Imhoff, G. L. Graff, L. Li, J. Hu, C. Wang, J. Xiao, G. Xia, V. V. Viswanathan, S. Baskaran, V. Sprenkle, X. Li, Y. Shao, B. Schwenzer, *Adv. Funct. Mater.* **2013**, 23, 929.
- [2] a) L. Suo, O. Borodin, T. Gao, M. Olguin, J. Ho, X. Fan, C. Luo, C. Wang, K. Xu, *Science* **2015**, 350, 938; b) Z. Li, D. Young, K. Xiang, W. C. Carter, Y. Chiang, *Adv. Energy Mater.* **2013**, 3, 290; c) C. D. Wessells, S. V. Peddada, R. A. Huggins, Y. Cui, *Nano Lett.* **2011**, 11, 5421; d) P. Saha, M. K. Datta, O. I. Velikokhatnyi, A. Manivannan, D. Alman, P. N. Kumta, *Prog. Mater. Sci.* **2014**, 66, 1; e) H. Pan, Y. Shao, P. Yan, Y. Cheng, K. S. Han, Z. Nie, C. Wang, J. Yang, X. Li, P. Bhattacharya, K. T. Mueller, J. Liu, *Nat. Energy* **2016**, 1, 16039; f) N. Zhang, F. Cheng, J. Liu, L. Wang, X. Long,

- X. Liu, F. Li, J. Chen, *Nat. Commun.* **2017**, *8*, 405; g) D. Kundu, B. D. Adams, V. Duffort, S. H. Vajargah, L. F. Nazar, *Nat. Energy* **2016**, *1*, 16119.
- [3] a) T. Gupta, A. Kim, S. Phadke, S. Biswas, T. Luong, B. J. Hertzberg, M. Chamoun, K. Evans-Lutterodt, D. A. Steingart, *J. Power Sources* **2016**, *305*, 22; b) L. Zhang, L. Chen, X. Zhou, Z. Liu, *Adv. Energy Mater.* **2015**, *5*, 1400930; c) Z. Jia, B. Wang, Y. Wang, *Mater. Chem. Phys.* **2015**, *149*, 601; d) M. H. Alfaruqi, V. Mathew, J. Gim, S. Kim, J. Song, J. P. Baboo, S. H. Choi, J. Kim, *Chem. Mater.* **2015**, *27*, 3609; e) P. Senguttuvan, S. Han, S. Kim, A. L. Lipson, S. Tepavcevic, T. T. Fister, I. D. Bloom, A. K. Burrell, C. S. Johnson, *Adv. Energy Mater.* **2016**, *6*, 1600826; f) M. H. Alfaruqi, V. Mathew, J. Song, S. Kim, S. Islam, D. T. Pham, J. Jo, S. Kim, J. P. Baboo, Z. Xiu, K. Lee, Y. Sun, J. Kim, *Chem. Mater.* **2017**, *29*, 1684.
- [4] Y. Wang, G. Cao, *Adv. Mater.* **2008**, *20*, 2251.
- [5] M. Ko, S. Chae, S. Jeong, P. Oh, J. Cho, *ACS Nano* **2014**, *8*, 8591.
- [6] H. Qiao, X. Zhu, Z. Zheng, L. Liu, L. Zhang, *Electrochem. Commun.* **2006**, *8*, 21.
- [7] Y. Oka, T. Yao, N. Yamamoto, *J. Solid State Chem.* **1990**, *89*, 372.
- [8] H. Li, T. Zhai, P. He, Y. Wang, E. Hosono, H. Zhou, *J. Mater. Chem.* **2011**, *21*, 1780.
- [9] C. Tsang, A. Manthiram, *J. Electrochem. Soc.* **1997**, *144*, 520.
- [10] D. Yang, A. Velamakanni, G. Bozoklu, S. Park, M. Stoller, R. D. Piner, S. Stankovich, I. Jung, D. A. Field, C. A. Ventrice Jr., R. S. Ruoff, *Carbon* **2009**, *47*, 145.
- [11] a) N. Zhang, F. Cheng, Y. Liu, Q. Zhao, K. Lei, Ch. Chen, X. Liu, J. Chen, *J. Am. Chem. Soc.* **2016**, *138*, 12894; b) G. Li, Z. Yang, Y. Jiang, W. Zhang, Y. Huang, *J. Power Sources* **2016**, *308*, 52;
- [12] P. Simon, Y. Gogotsi, *Nat. Mater.* **2008**, *7*, 845.
- [13] J. Y. Luo, W. J. Cui, P. He, Y. Y. Xia, *Nat. Chem.* **2010**, *2*, 760.
- [14] W. Tang, Y. Zhu, Y. Hou, L. Liu, Y. Wu, K. P. Loh, H. Zhang, K. Zhu, *Energy Environ. Sci.* **2013**, *6*, 2093.
- [15] R. Raccichini, A. Varzi, S. Passerini, B. Scrosati, *Nat. Mater.* **2015**, *14*, 271.
- [16] G. Kucinskis, G. Bajars, J. Kleperis, *J. Power Sources* **2013**, *240*, 66.
- [17] I. Mjejri, N. Etteyeb, F. Sediri, *J. Alloys Compd.* **2014**, *611*, 372.
- [18] K. Zhu, X. Yan, Y. Zhang, Y. Wang, A. Su, X. Bie, D. Zhang, F. Du, C. Wang, G. Chen, Y. Wei, *ChemPlusChem* **2014**, *79*, 447.
- [19] F. D. Hardcastle, I. E. Wachs, *J. Phys. Chem.* **1991**, *95*, 5031.
- [20] S. Ni, G. Zhou, S. Lin, X. Wang, Q. Pan, F. Yang, D. He, *Mater. Lett.* **2009**, *63*, 2459.
- [21] W. W. Rudolph, C. C. Pye, *J. Solution Chem.* **1999**, *28*, 1045.
- [22] M. R. Lukatskaya, O. Mashtalir, C. E. Ren, Y. Dall'Agnese, P. Rozier, P. L. Taberna, M. Naguib, P. Simon, M. W. Barsoum, Y. Gogotsi, *Science* **2013**, *341*, 1502.
- [23] D. S. Charles, M. Feyngenson, K. Page, J. Neuefeind, W. Xu, X. Teng, *Nat. Commun.* **2017**, *8*, 15520.
- [24] D. Buchholz, L. G. Chagas, C. Vaalma, L. Wu, S. Passerini, *J. Mater. Chem. A* **2014**, *2*, 13415.
- [25] C. T. Lin, D. P. Chen, P. Lemmens, X. N. Zhang, A. Maljuk, P. X. Zhang, *J. Cryst. Growth* **2005**, *275*, 606.
- [26] A. B. Yankovich, B. Berkels, W. Dahmen, P. Binev, S. I. Sanchez, S. A. Bradley, A. Li, I. Szlufarska, P. M. Voyles, *Nat. Commun.* **2014**, *5*, 4155.
- [27] Y. Xu, H. Bai, G. Lu, C. Li, G. Shi, *J. Am. Chem. Soc.* **2008**, *130*, 5856.
- [28] Y. Li, Z. Hu, Y. Ding, J. Kan, *Int. J. Electrochem. Sci.* **2016**, *11*, 1898.